Kinetic Pathways of Fast Lithium Transport in Solid Electrolyte Interphases with Discrete Inorganic Components

Yikang Yu [1,2, +], Hyeongjun Koh [3, +], Zisheng Zhang[5, +], Zhenzhen Yang [4], Anastassia N. Alexandrova [5,6], Mangilal Agarwal [1], Eric A. Stach [3, *], Jian Xie [1, *]

[1]Department of Mechanical and Energy Engineering, Purdue School of Engineering and Technology, Indiana University – Purdue University Indianapolis, Indianapolis, IN, 46202, United States

[2] School of Mechanical Engineering, Purdue University, West Lafayette, IN, 47907, United States

[3] Department of Materials Science and Engineering and Laboratory for Research on the Structure of Matter, University of Pennsylvania, Philadelphia, PA, 19104, United States

[4] Chemical Sciences and Engineering Division, Argonne National Laboratory, Lemont, IL, 60439, United States

[5] Department of Chemistry and Biochemistry and [6] California NanoSystems Institute, University of California, Los Angeles, Los Angeles, CA, 90095, United States

[+] These authors contributed equally to this work.

Email: jianxie@iupui.edu; stach@seas.upenn.edu

Experimental Methods

Materials. Battery-grade $LiPF_6$, ethylene carbonate (EC), and ethyl methyl carbonate (EMC) were purchased from Novolyte Technologies. $LiNO_3$ (99%) and Niobium oxide (99.5%) were provided by Alfa Aesar. For electrode and coin cell preparation, Li foil (99.9%, 15.8 mm) and Super P conductive carbon were supplied by MTI Corporation while the sodium carboxymethyl cellulose (CMC) binder was purchased from Sigma-Aldrich.

Electrolyte and electrode preparation. The EC-based conventional electrolyte was prepared by dissolving 1.2 M $LiPF_6$ in EC-EMC (3:7 by mass) mixed solvent inside a Ar-filled glovebox. $LiNO_3$ added electrolyte was obtained by adding excess $LiNO_3$ additives into the EC-based electrolyte to form a $LiNO_3$ saturated electrolyte (~0.01 M). The Nb_2O_5 anodes were obtained by slurry coating on Cu foil, which consists of 70 wt.% Nb_2O_5, 20 wt.% Super P and 10 wt.% CMC as binder. It is worth noting that DI water was used for the slurry preparation. The areal mass loading was about 3.0 mg cm^{-2}. The Nb_2O_5 electrodes were punched into disks with a diameter of 15 mm after drying at a vacuum oven overnight with a temperature of 60 °C. The $Li_4Ti_5O_{12}$ and $LiFePO_4$ (LFP) electrodes were prepared by slurry coating on Cu and Al foil respectively, which consists of 80% wt.% active materials, 10 wt.% Super P and 10 wt.% polyvinylidene fluoride as binder. The full cell of LFP/Nb_2O_5 were constructed by controlling the negative/positive ratio (N/P ratio) to 1.03.

Materials characterization. For ex-situ analysis, cycled coin cells were disassembled in the glovebox to collect the Nb_2O_5 electrode and then were further washed by EMC to remove residual electrolytes. These electrodes were dried and sealed in glass vials for further characterization. SEM images and selected area of energy dispersive X-ray spectroscopy were obtained using field emission scanning electron microscope (FESEM, JEOL 7800). XPS data was acquired using PHI 5000 VersaProbe II system attached with an argon-filled glovebox to avoid contamination of moisture and air. The reported element atomic concentrations were calculated from survey scans. The cycled Nb_2O_5 electrodes (1-20 cycles, 10 C) were examined by X-ray powder diffraction facilities (Cu, Kα, Bruker D8 Discover). To observe the SEI directly attached to the Nb_2O_5 particles (direct SEI), the synthesized slurry electrodes on Cu foils were mildly sonicated in a vial containing 0.5 ml dimethyl carbonate (DMC) for 10 seconds to disperse the electrode particles. Subsequently, the dispersed particles were drop-casted to lacey carbon TEM grids (Ted Pella) followed by drying under evacuated antechamber for 10 minutes. Once the samples were dried, they were transferred in a sealed container before they were plunged into liquid nitrogen. The containers were cut under liquid nitrogen to minimize any air contact during the transfer. The samples were finally placed into the cryo TEM holder (Cryogenic Transfer holder 3500, Gatan) at around -170 °C. A shutter

designed to prevent any moisture from condensing on the TEM samples was closed while it was inserted into a TEM column and was opened after a vacuum level in the TEM column was stabilized. HR-TEM characterizations were carried out by a JEOL F200 operated at 200 KV and cryo TEM images were acquired with a OneView Camera (Gatan) at a dose rate of ~ 700 e^-/ $Å^{-2}$/s for 0.5 seconds. EELS data were collected with a JEOL NEOARM instrument operated at 200 kV in scanning transmission electron microscopy (STEM) mode. A Gatan imaging filter (GIF) aperture of 5 mm was used, and the EELS data were obtained with a Gatan Ultrascan camera. The pixel time for the EELS mapping was 0.5 ms for Li K-edge and the other elements were all acquired at 10 ~ 30 ms pixel time. Moreover, pure porous SEI structures without Nb_2O_5 particle were investigated by cryo-STEM using an established method[1]. In this coin cell configuration, one piece of copper TEM grid was placed on the Cu current collector foil as working electrode with a Li foil as reference/counter electrode. The SEI is deposited by discharging and charging the cell with the same voltage range as Nb_2O_5 anode for 10 cycles (1.0-3.0 V vs. Li^+/Li) at a small current (0.01 mA).

Electrochemical tests. All of the electrochemical tests were performed using CR2032 type coin cell, in which Li foils (0.5 mm) were used as the counter/reference electrode and as-prepared Nb_2O_5 electrodes were used as the working electrode. One piece of Celgard 2400 polypropylene separator and 50 μL of as prepared electrolytes were used in each cell. The cut-off voltage was controlled from 1.0 to 3.0 V (vs. Li^+/Li). The cyclic voltammetry analysis (0.5 mV/s) was conducted using a Solartron potentiostat with a range of 1.0 to 3.0 V (vs. Li^+/Li) as well while the LSV scan (0.5 mV/s) were performed using Cu foil as working electrode and Li foil as counter/reference electrode within the voltage range of 2.0-1.0 V (vs. Li^+/Li). The LFP/Nb_2O_5 full cells were cycled within the voltage range of 0.8 to 2.8 V at different C-rate condition. The electrochemical impedance spectra (EIS) were conducted with a AC voltage of 5 mV in the frequency range from 1 MHz to 0.01 Hz (Solartron Model SI 1287). The EIS is collected after the cell is charged to 3.0V (vs. Li+/Li) after enough time to rest (>24 h), and the OCV is around 2.2V. Galvanostatic charge and discharge were controlled by a LAND-CT2001 battery testing instrument with a determined C-rate (1 C = 200 mA/g for Nb_2O_5 anodes, 1 C = 175 mA/g for LTO anodes, 1 C = 170 mA/g for LFP/Nb_2O_5 full cells). The current was calculated based on the mass loading of each electrode. The Li-Li symmetrical cells were assembled by depositing 10 mAh/cm^2 on a Cu current collector as working electrode with a Li foil as reference/counter electrode to study the influence of $LiNO_3$ for Li metal anode at difference current density (e.g. 0.1 mA/cm^2 to 2 mA/cm^2).

Density functional theory (DFT) calculations. Li_2O bulk is modeled by a 2×2×2 supercell of composition $Li_{64}O_{32}$. Li_2O surface is modeled by a 6×6 slab of stoichiometric (111) termination with a 15 Å vacuum gap in z direction, of composition $Li_{144}O_{72}$. Nb_2O_5 surface is modeled by a stoichiometric (110) termination with a 15 Å vacuum gap in z direction, of composition $Nb_{56}O_{140}$. All lattice parameters and crystal structures of the unit cells were taken from Materials Project database [2]. The structure of partially desolvated Li^+ ions are built based on the contact ion pairs (CIP) and solvation separated ion pairs (SSIP) solvation structures reported in ref [3]. The in-electrolyte diffusion of Li^+ ion is modeled by the hopping of a Li^+ between two sites of two EMC anions.

All DFT calculations are performed with the PBE functional[4] and PAW pseudopotentials[5] using the VASP program[6-9]. D3 correction is used to account for the dispersion interactions.[10] Implicit solvation model, as implemented in VASPsol, is use for all non-solid-state calculations, with a dielectric constant of 18.5[11, 12]. The convergence criteria are set to 10^{-5} eV for the SCF iterations and 2×10^{-2} eV/Å for forces during geometry optimizations. A single Γ-centered *k*-point is used to sample the Brillouin zone due to relatively large system size. The cutoff energy for the kinetic energy of the plane-waves is 400 eV. A Gaussian smearing of 0.1 eV broadening is used throughout. The transition states (TS) are obtained using climbing image nudged elastic band (CI-NEB) method[13], starting from a band interpolated between the initial state (IS) and final state (FS). Each TS geometry has been calculated to have only one imaginary mode.

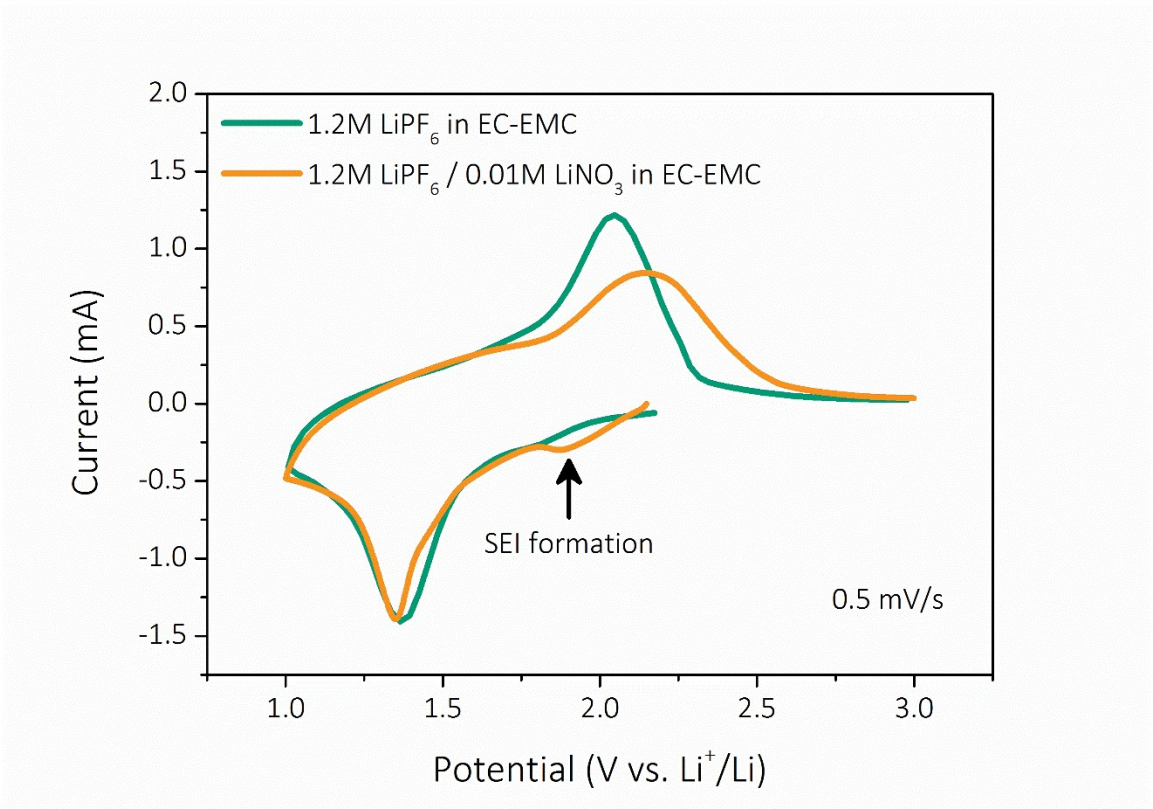

Figure S1. Initial cyclic voltammetry curves of H-Nb_2O_5 in conventional EC-based electrolyte (1.2 M $LiPF_6$ in EC-EMC) and $LiNO_3$ added EC-based electrolyte (1.2 M $LiPF_6$ / 0.01 M $LiNO_3$ in EC-EMC).

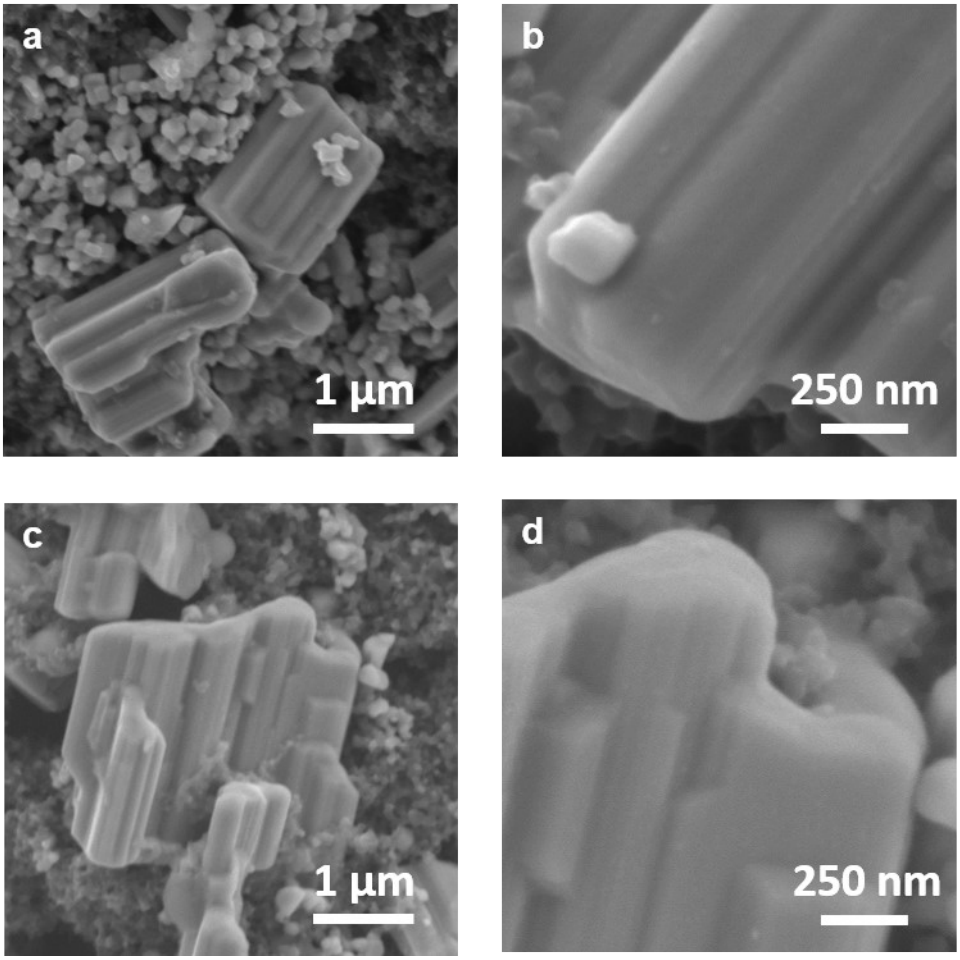

Figure S2. SEM images of H-Nb_2O_5 cycled in conventional EC-based electrolyte (a-b) and $LiNO_3$ added EC-based electrolyte (c-d).

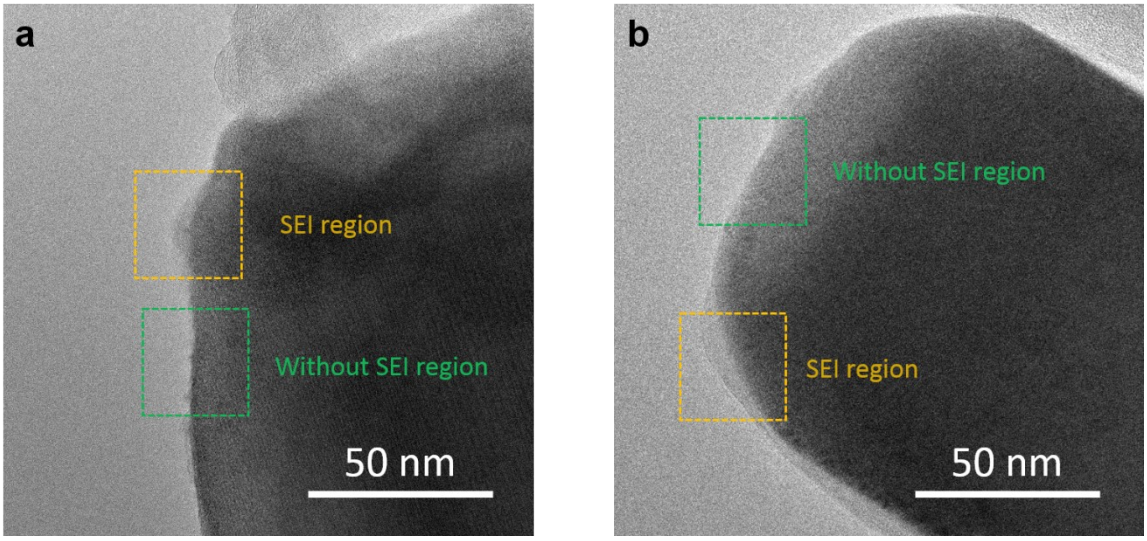

Figure S3. Low magnification Cryo-TEM images reveal the porous SEI on H-Nb_2O_5 after cycling in conventional EC-based electrolyte (a) and $LiNO_3$ added EC-based electrolyte (b).

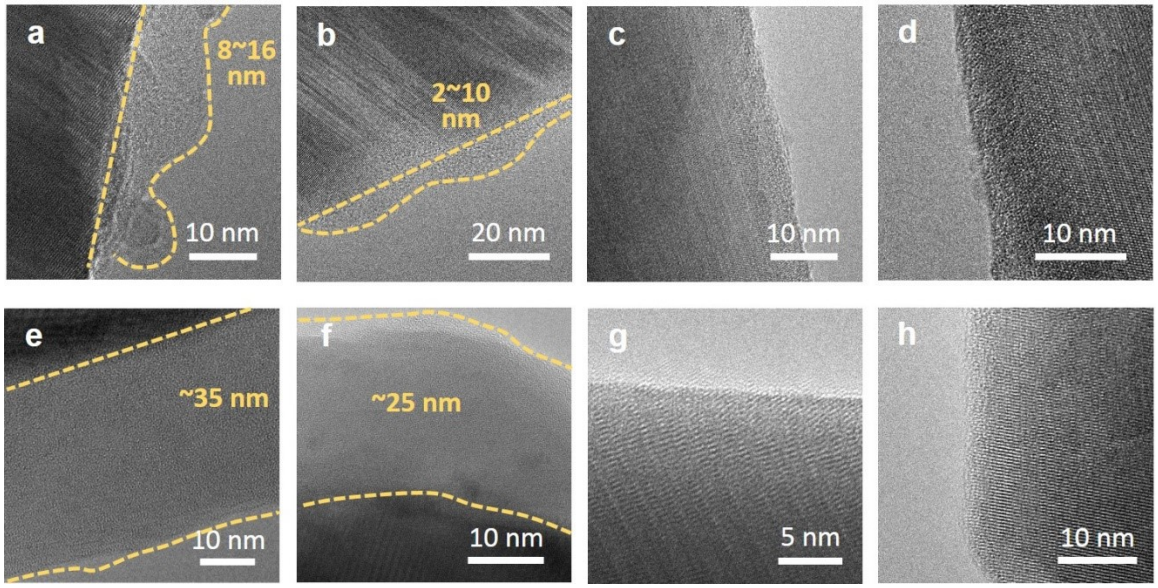

Figure S4. Cryo-TEM images reveal the SEI thickness on H-Nb_2O_5 after cycling in conventional EC-based electrolyte (a-d) and $LiNO_3$ added EC-based electrolyte (e-h).

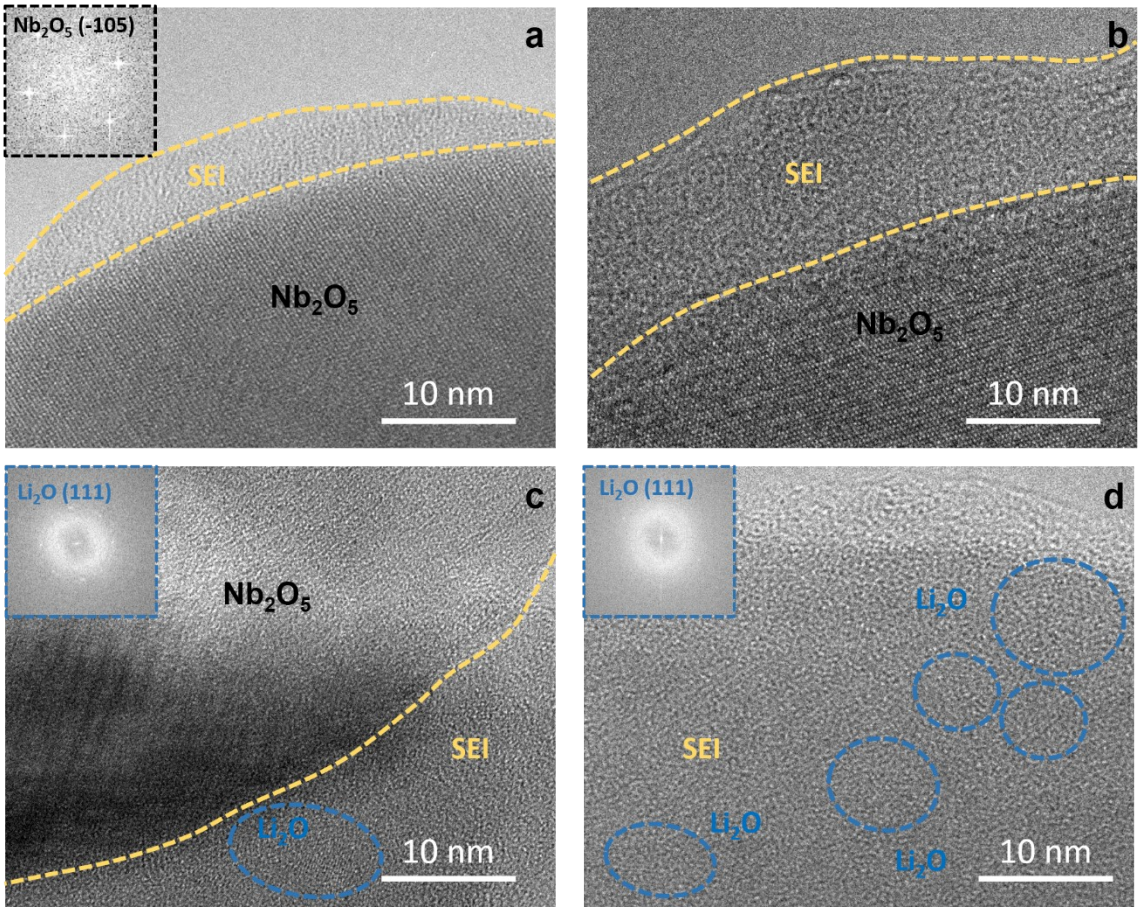

Figure S5. Cryo-TEM images reveal the direct SEI structures on H-Nb_2O_5 after cycling in conventional EC-based electrolyte (a-b) and $LiNO_3$ added EC-based electrolyte (c-d).

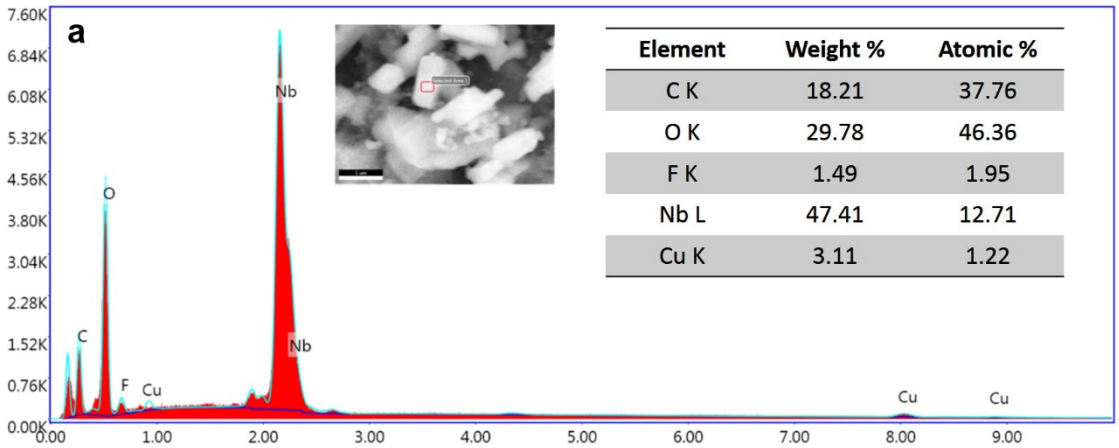

Element	Weight %	Atomic %
C K	18.21	37.76
O K	29.78	46.36
F K	1.49	1.95
Nb L	47.41	12.71
Cu K	3.11	1.22

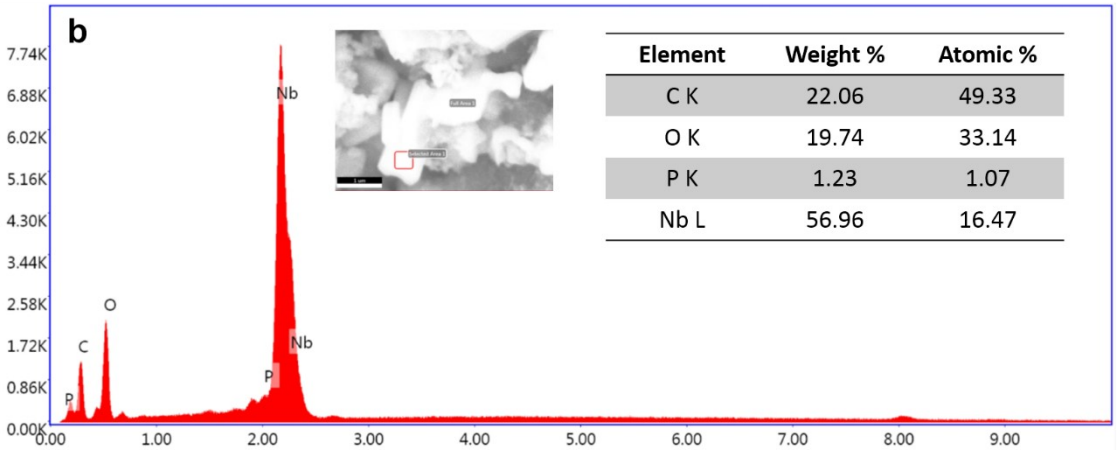

Element	Weight %	Atomic %
C K	22.06	49.33
O K	19.74	33.14
P K	1.23	1.07
Nb L	56.96	16.47

Figure S6. Selected area of energy dispersive X-ray spectroscopy (EDS) on H-Nb_2O_5 surface after cycling in $LiNO_3$ added EC-based electrolyte (a) and neat EC-based electrolyte (b) and corresponding element atomic ratio on Nb_2O_5 particle surface. Quantification by standardless methods is shown. These methods are not likely to be as accurate as indicated by the number of significant figures but do certainly capture the general trends in composition within a percent or two.

Table S1. Element atomic percentage obtained from X-ray photoelectron spectroscopy (XPS), which presents a broader range of element distribution compared with SEM EDS analysis.

Element	H-Nb_2O_5 cycled without $LiNO_3$	H-Nb_2O_5 cycled with $LiNO_3$
Li 1s	24.25%	15.35%
C 1s	26.26%	31.77%
N 1s	0.00%	1.14%
O 1s	38.38%	40.60%
F 1s	10.27%	10.94%
Nb 3d	0.83%	0.20%

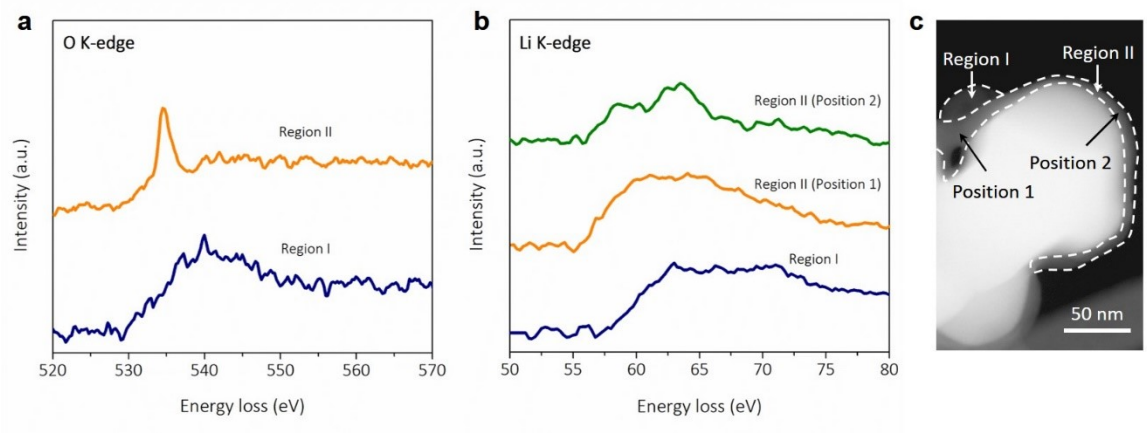

Figure S7. Cryogenic electron energy loss spectra of direct SEI structures from H-Nb_2O_5 cycled in $LiNO_3$ added EC-based electrolyte. (a-b) EELS spectra of O K-edge and Li K-edge from corresponding position (c).

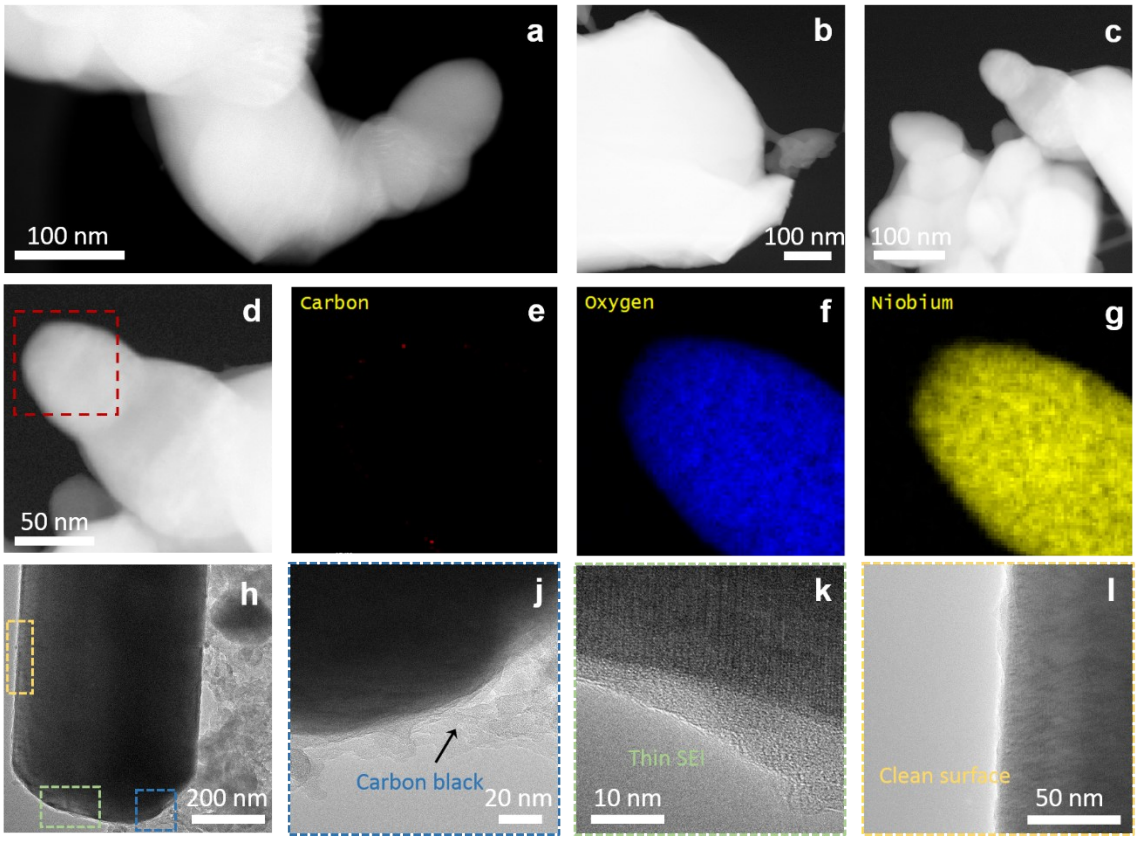

Figure. S8. Cryo-(S)TEM investigations of the SEI structures over Nb_2O_5 after 200 cycles at 10 C in neat EC-based electrolyte. HAADF cryo-STEM images of SEI structures after 200 cycles at three different locations (a-d) and representative EELS elemental maps of the direct SEI (e-g). HRTEM images indicates the thickness of the direct SEI at different area (j-l) on a Nb_2O_5 particle surface (h). Note that the locations for HAADF cryo-STEM images with EELS elemental maps (a-g) and high resolution TEM (h-l) are different locations since they are taken from two different TEM instruments.

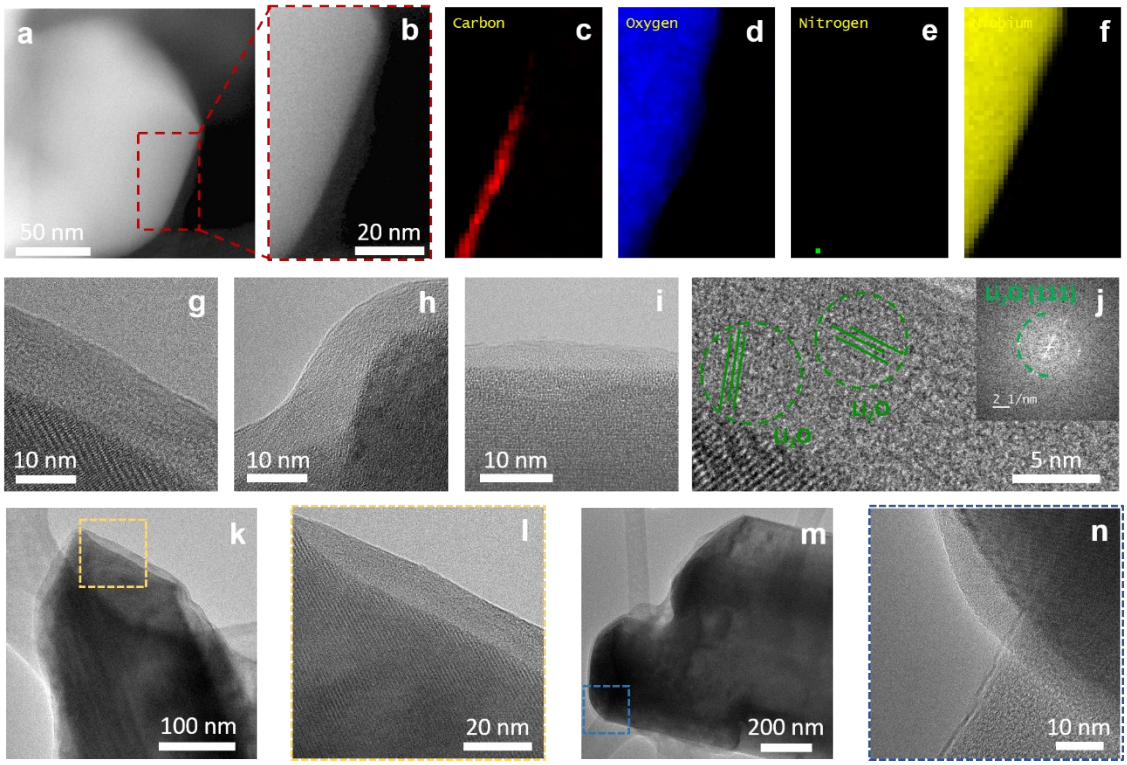

Figure. S9. Cryo-(S)TEM investigations of the SEI structures over Nb_2O_5 after 200 cycles at 10 C in $LiNO_3$ added EC-based electrolyte. HAADF cryo-STEM image of SEI structures after 200 cycles (a-b) and its EELS elemental maps (c-f) of the direct SEI. HRTEM images show the SEI with 20 nm in the thickness at different areas (g-i). (j) A magnified SEI image and its FFT inset indicates Li2O distributions after cycles. Coverage of the direct SEI on Nb_2O_5 surface was presented on two different particles (k-l, m-n). Note that the locations for HAADF cryo-STEM images with EELS elemental maps (a-f) and high resolution TEM (g-n) are different locations since they are taken from two different TEM instruments.

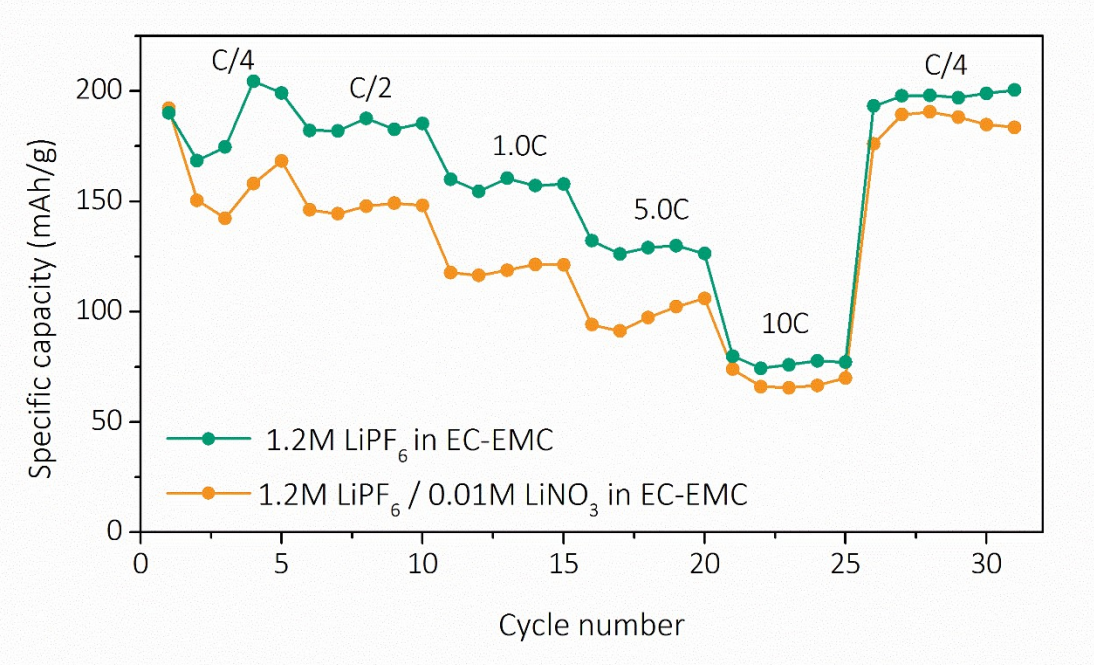

Figure S10. C-rate of H-Nb_2O_5 with cycling in conventional EC-based electrolyte and $LiNO_3$ added EC-based electrolyte (1C=200 mA/g).

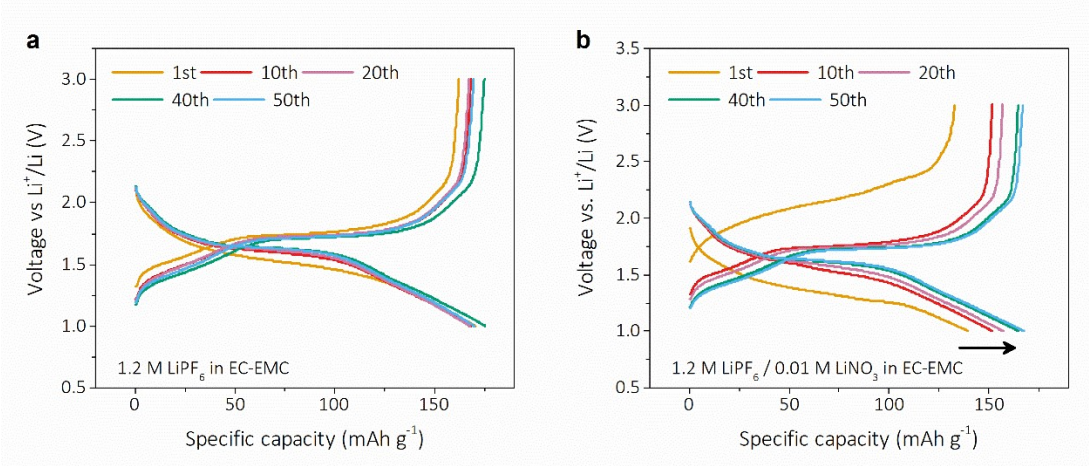

Figure S11. Galvanostatic charge and discharge curve of H-Nb_2O_5 with cycling in conventional EC-based electrolyte (a) and $LiNO_3$ added EC-based electrolyte (b) at 1 C rate for the activation cycles.

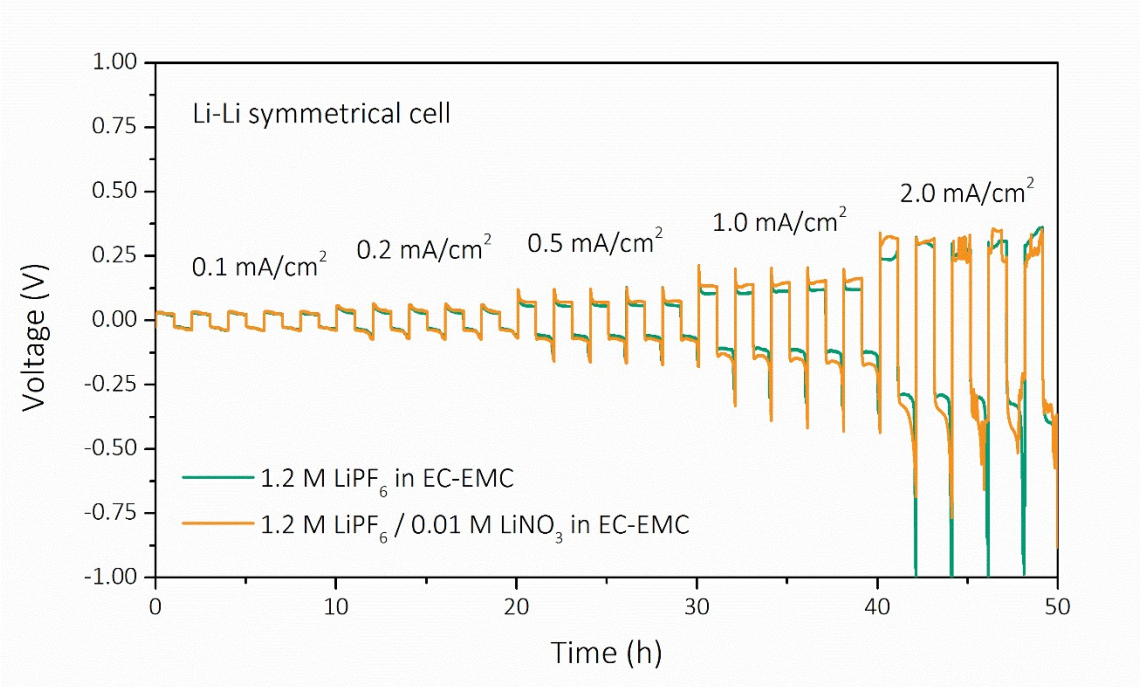

Figure S12. Voltage profiles of Li-Li symmetrical cells at different current density from 0.1 mA/cm^2 to 2.0 mA/cm^2, which presents the Li metal anode performance within the current range for H-Nb_2O_5 charge and discharge (C/4 to 10C). The similar overpotential between EC-based electrolyte and $LiNO_3$ added EC-based electrolyte confirms that the existence of $LiNO_3$ at a limited amount (~0.01M) in electrolyte does not have a significant effect on Li metal anode side, while the H-Nb_2O_5 electrode side dominates the half-cell performance.

Table S2. The comparison of Li diffusion coefficient in different battery materials and representative SEI components.

Materials	Diffusion coefficient	Ref.
Graphite	~10^{-7}-10^{-6} cm^2 s^{-1} parallel to graphene plane and ~10^{-11} cm^2 s^{-1} along grain boundaries. (experimental)	14
Anatase TiO_2	4.7×10^{-12} cm^2 s^{-1} (experimental)	15
$Li_4Ti_5O_{12}$	1.3×10^{-11} cm^2 s^{-1} (experimental)	15
Nb_2O_5	7.547×10^{-13} cm^2 s^{-1} (experimental)	16
Si	10^{-14} – 10^{-10} cm^2 s^{-1}(experimental)	17
Li_2O	4.01×10^{-14} cm^2 s^{-1} (300 K) (MD simulation)	18
LiF	3.93×10^{-14} cm^2 s^{-1} (300 K) (MD simulation)	18
Li_2CO_3	3.30×10^{-14} cm^2 s^{-1} (300 K) (MD simulation)	18
Dilithium ethylene dicarbonate	~10^{-14} cm^2 s^{-1} (333 K) (experimental)	19

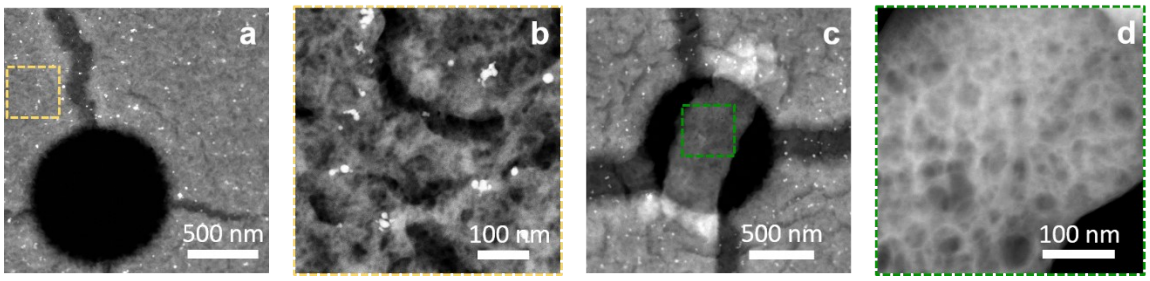

Figure S13. HAADF cryo-STEM images of pore SEI structure without Nb_2O_5 formed using neat EC-based electrolyte at two different locations (a-b, c-d). Both locations demonstrate a very similar pore structure, and the slight difference is come from the different thickness of the SEI. Note that some cracks of the SEI in (a-c) may cause by cell disassembly process.

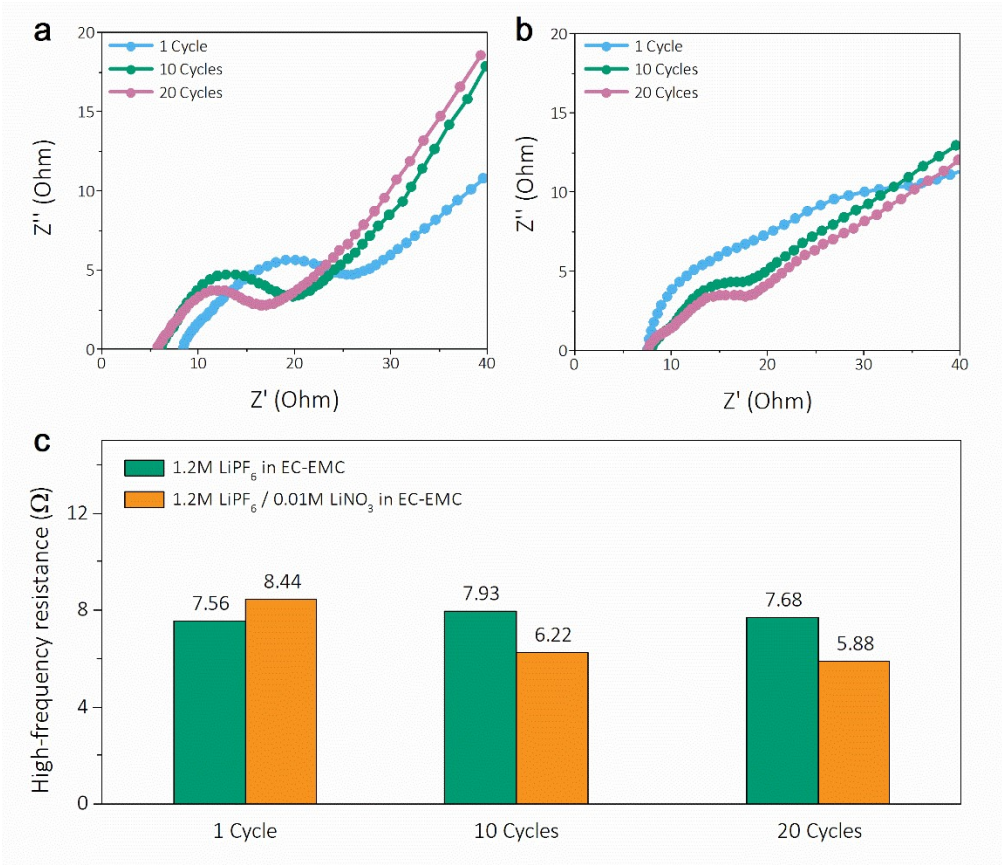

Figure S14. Nyquist plots of H-Nb_2O_5 after cycling (1 Cycle, 10 Cycles, and 20 Cycles) in conventional EC-based electrolyte (a) and $LiNO_3$ added EC-based electrolyte (b) and comparison of their high-frequency resistance (c), which presents the wetting degree between the electrode with electrolytes.

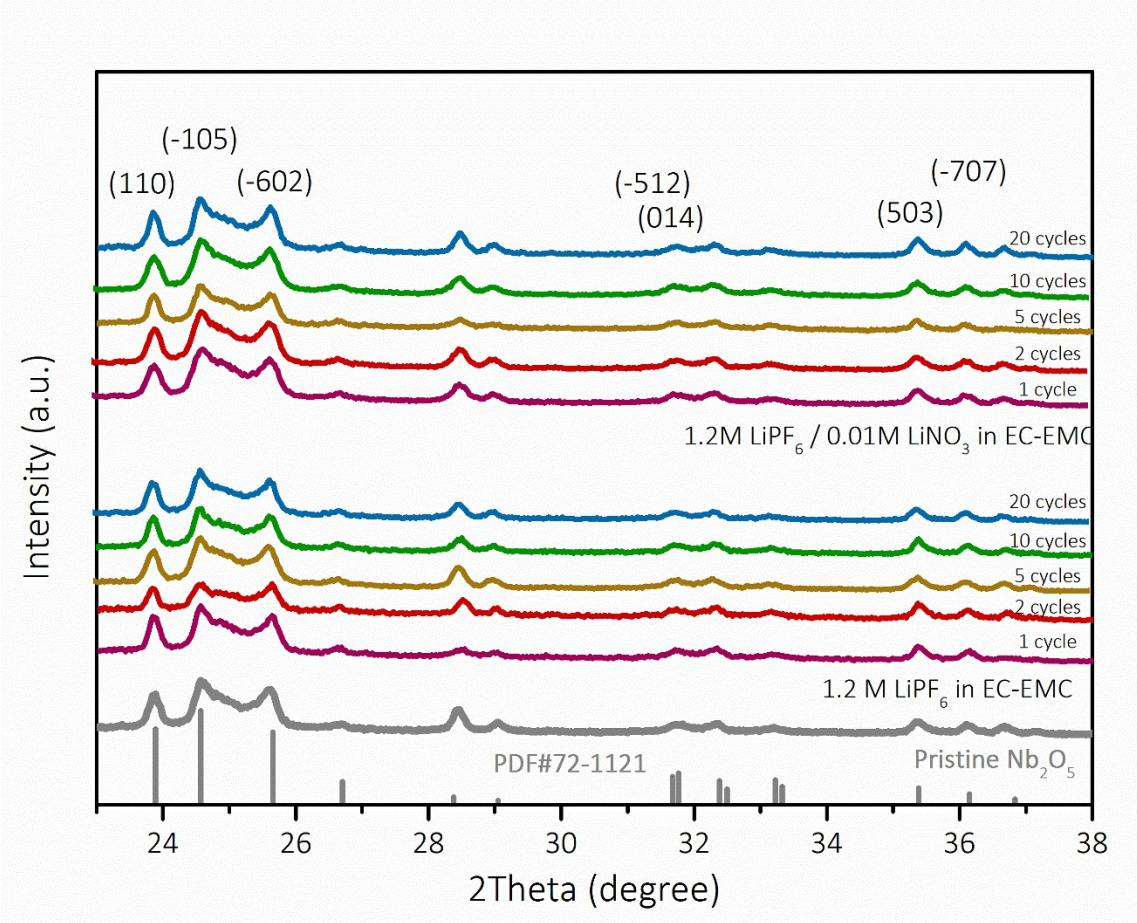

Figure S15. Ex-situ XRD patterns of H-Nb_2O_5 after cycling (1 cycle, 2 cycles, 5 cycles, 10 cycles and 20 Cycles, 10C) in conventional EC-based electrolyte and $LiNO_3$ added EC-based electrolyte. It worth noting that the XRD patterns were calibrated using (-105) peak to avoid the error during the sample preparation and measurement (e.g. sample height), which means the expansion (peak left shit) or shrink (peak right shit) of lattice plane (XRD peak) is relative to the (-105) peak.

Table S3. d-spacing changes of two representative lattice plane with cycling

Cycle Number	H-Nb_2O_5 cycled without $LiNO_3$	H-Nb_2O_5 cycled with $LiNO_3$
Lattice Plane	(110)	
Pristine	0.3742 nm	0.3742 nm
1 Cycle	0.3750 nm	0.3750 nm
2 Cycles	0.3753 nm	0.3747 nm
5 Cycles	0.3743 nm	0.3747 nm
10 Cycles	0.3750 nm	0.3747 nm
20 Cycles	0.3750 nm	0.3747 nm
Lattice Plane	(013)	
Pristine	0.3156 nm	0.3156 nm
1 Cycle	0.3143 nm	0.3148 nm
2 Cycles	0.3143 nm	0.3148 nm
5 Cycles	0.3148 nm	0.3145 nm
10 Cycles	0.3143 nm	0.3143 nm
20 Cycles	0.3143 nm	0.3143 nm

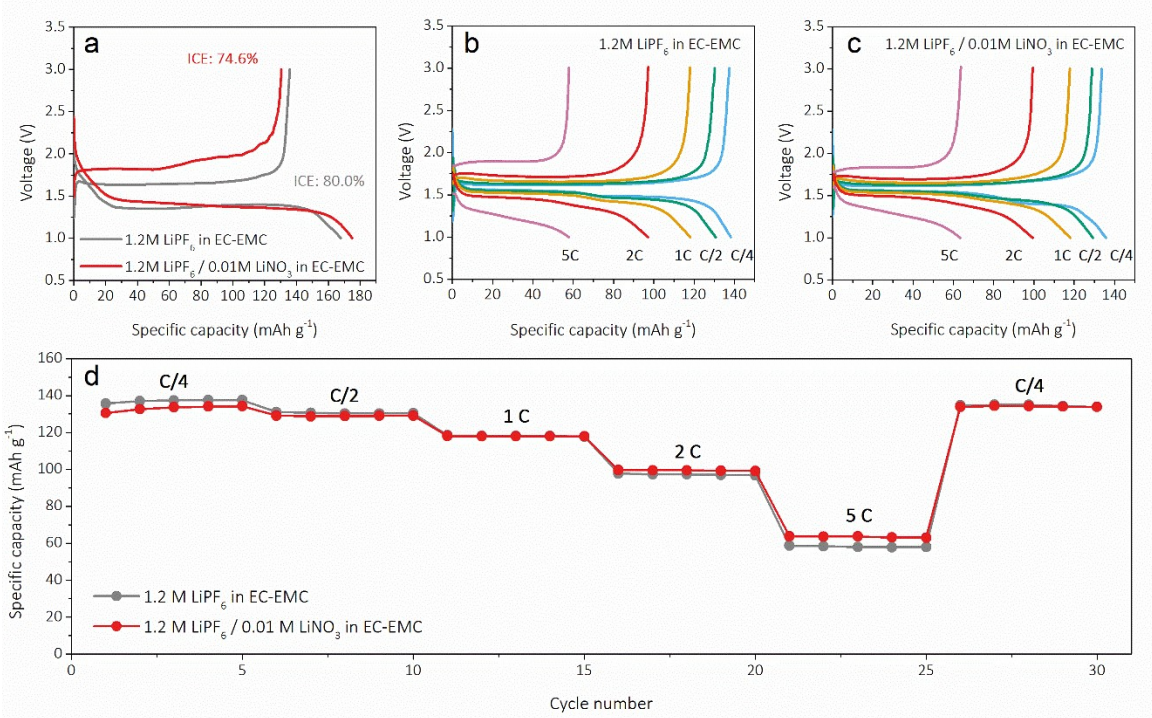

Figure. S16. C-rate cycling of $Li_4Ti_5O_{12}$ (LTO) anodes. (a) Initial cycle of the LTO anode in neat EC-based electrolyte and $LiNO_3$ added EC-based electrolyte (C/4) and corresponding charge/discharge curve at different C-rate in these two electrolytes as indicated (b-c). (d) C-rate performance at different cycling rate.

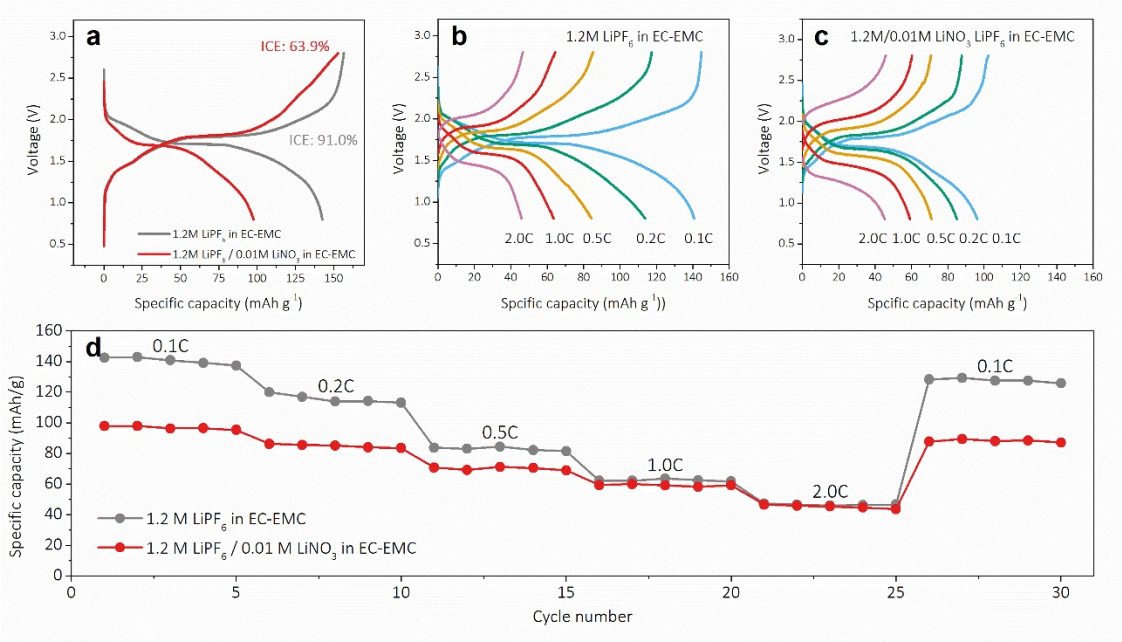

Figure. S17. C-rate cycling of LFP/Nb_2O_5 full cells. (a) Initial cycle of the LFP/Nb_2O_5 full cells in neat EC-based electrolyte and $LiNO_3$ added EC-based electrolyte (0.1C) and corresponding charge/discharge curve at different C-rate in these two electrolytes as indicated (b-c). (d) C-rate performance at different cycling rate.

Reference

1. F. Lin, D. Nordlund, T.-C. Weng, Y. Zhu, C. Ban, R. M. Richards and H. L. Xin, *Nature communications*, 2014, **5**, 3358.
2. S. P. Ong, W. D. Richards, A. Jain, G. Hautier, M. Kocher, S. Cholia, D. Gunter, V. L. Chevrier, K. A. Persson and G. Ceder, *Computational Materials Science*, 2013, **68**, 314-319.
3. T. Hou, K. D. Fong, J. Wang and K. A. Persson, *Chemical science*, 2021, **12**, 14740-14751.
4. J. P. Perdew, K. Burke and M. Ernzerhof, *Physical review letters*, 1996, **77**, 3865.
5. G. Kresse and D. Joubert, *Physical review b*, 1999, **59**, 1758.
6. G. Kresse and J. Furthmüller, *Computational materials science*, 1996, **6**, 15-50.
7. G. Kresse and J. Furthmüller, *Physical review B*, 1996, **54**, 11169.
8. G. Kresse and J. Hafner, *Physical review B*, 1993, **47**, 558.
9. G. Kresse and J. Hafner, *Physical Review B*, 1994, **49**, 14251.
10. S. Grimme, J. Antony, S. Ehrlich and H. Krieg, *The Journal of chemical physics*, 2010, **132**, 154104.
11. K. Mathew, V. Kolluru, S. Mula, S. N. Steinmann and R. G. Hennig, *The Journal of chemical physics*, 2019, **151**.
12. J. Self, N. T. Hahn and K. A. Persson, *Energy & Environmental Materials*, 2020, e12494.
13. G. Henkelman, B. P. Uberuaga and H. Jónsson, *The Journal of chemical physics*, 2000, **113**, 9901-9904.
14. K. Persson, V. A. Sethuraman, L. J. Hardwick, Y. Hinuma, Y. S. Meng, A. van der Ven, V. Srinivasan, R. Kostecki and G. Ceder, *The Journal of Physical Chemistry Letters*, 2010, **1**, 1176-1180.
15. M. Wagemaker, R. van de Krol, A. P. Kentgens, A. A. Van Well and F. M. Mulder, *Journal of the American Chemical Society*, 2001, **123**, 11454-11461.
16. Z. Liu, W. Dong, J. Wang, C. Dong, Y. Lin, I.-W. Chen and F. Huang, *Iscience*, 2020, **23**, 100767.
17. H. Wang, X. Ji, C. Chen, K. Xu and L. Miao, *AIP Advances*, 2013, **3**, 112102.
18. L. Benitez and J. M. Seminario, *Journal of The Electrochemical Society*, 2017, **164**, E3159.
19. O. Borodin, G. V. Zhuang, P. N. Ross and K. Xu, *The Journal of Physical Chemistry C*, 2013, **117**, 7433-7444.